Paired Interactions of Magnetic Millirobots in Confined Spaces Through Data-Driven Disturbance Rejection Control Under Global Input

Shihao Zhong, Siyu Guo, Tao Sun, Hen-Wei Huang, Qing Shi, *Senior Member, IEEE*, Qiang Huang, *Fellow, IEEE*, Toshio Fukuda, *Life Fellow, IEEE*, and Huaping Wang, *Member, IEEE*

***Abstract*—Owing to their high task efficiency and load capacity in closed space operations, multiple millirobots system has drawn extensive attention recently. However, the limited global magnetic fields and nonlinear interactions between individual robots make it challenging to control multiple millirobots in close proximity to each other, resulting in difficulty in achieving accurate paired interactions. Here, we propose a paired interactive control method for multiple millirobots, which enables the precise formation of two millirobots within a multiple millirobot system. The paired interactive motion is modeled within a singular point tracking framework to facilitate the implementation of an independent control strategy for multiple microrobots. Then, a data-driven actuation-movement mapping model for two millirobots is established as a nonlinear inversion controller, enabling the control system to rapidly achieve the desired state. To eliminate residual errors, a feedback controller is designed based on the active disturbance rejection concept, which estimates and eliminates generalized disturbances via an extended state observer. The control method is validated by accurately achieving planar formations via two millirobots both in isolation and within a multiple millirobot system, in which the root mean square error is less than 3% of the single-robot length.**

***Index Terms*—Magnetic actuation, multiple microrobot system, paired interactive control, underactuated control at small scales.**

Received 9 September 2024; revised 7 November 2024; accepted 19 December 2024. Date of publication 15 January 2025; date of current version 30 December 2025. Recommended by Technical Editor N. Motoi and Senior Editor K. Oldham. This work was supported in part by the National Key Research and Development Program of China under Grant 2023YFB4705400, in part by the National Natural Science Foundation of China under Grant 62222305 and Grant 62088101, and in part by the BIT Research and Innovation Promoting Project under Grant 2024YCXY007. *(Corresponding authors: Tao Sun; Huaping Wang.)*

Shihao Zhong and Siyu Guo are with the Intelligent Robotics Institute, School of Mechatronical Engineering, Beijing Institute of Technology, Beijing 100081, China (e-mail: 3120235409@bit.edu.cn; 1120201272@bit.edu.cn).

Tao Sun, Qing Shi, Qiang Huang, and Huaping Wang are with the Key Laboratory of Biomimetic Robots and Systems, Ministry of Education, Beijing Institute of Technology, Beijing 100081, China (e-mail: 6120200193@bit.edu.cn; shiqing@bit.edu.cn; qhuang@bit.edu.cn; wanghuaping@bit.edu.cn).

Hen-Wei Huang is with the School of Electrical and Electronic Engineering, LKC School of Medicine, Nanyang Technological University, Singapore 639798 (e-mail: henwei.huang@ntu.edu.sg).

Toshio Fukuda is with the Department of Micronano Systems Engineering, Nagoya University, Nagoya 464-8603, Japan (e-mail: tofukuda@nifty.com).

This article has supplementary material provided by the authors and color versions of one or more figures available at https://doi.org/10.1109/TMECH.2024.3521085.

Digital Object Identifier 10.1109/TMECH.2024.3521085

I. Introduction

MILLIROBOTS, remotely controlled by external magnetic fields, exhibit flexible mobility in narrow and confined spaces, drawing extensive attention for their potential in micromanipulation and biomedical applications [1], [2] [3], [4]. The successful completion of these tasks necessitates a high level of precision in the automatic motion of millirobots. In recent years, researchers have developed several efficient closed-loop motion control methods [5], [6], [7], [8], [9], [10] including model-based, model-free, and geometry-based approaches, to govern the movement of individual magnetic millirobots. These advancements have enabled the precise movement of individual magnetic robots within complex environments. To handle more complex tasks, simultaneous enhancements in load capacity, task efficiency, and fault tolerance are necessary. In this context, cooperation among multiple or even groups of millirobots has emerged as an optimal solution [11], [12], [13], for example, collective millirobots can generate azimuthal flows around themselves for targeted active drug or other cargo delivery and for the manipulation of cells within a microfluidic chip [14], [15]. However, in contrast to industrial robots with independent drive and sensing capabilities, within the same magnetic field, multiple millirobots are steered by a common control signal and lack the means to communicate among themselves [16], [17], [18]. Achieving precise collaborative motion control for multiple magnetic millirobot systems has become a significant challenge in small-scale robotics research [19].

Researchers have focused on fundamental paired interactive control to facilitate the collaborative operation of multiple magnetic millirobots. The interaction between two magnetic millirobots can be realized through the differential design of a millirobot ontology, multiple magnetic propulsion devices,

and auxiliary intervention equipment. The different geometric shapes and magnetization properties of multiple millirobots can result in varying velocities and motion directions under common magnetic control signals [18], [20], [21], [22]. With different responses, the customization of control signal input sequences enables the realization of interactive control among individual robots while simultaneously ensuring adequate spacing to avoid mutual magnetic distraction. Through a distributed array of electromagnetic coil systems, individual or collective control of these coils can generate high-intensity driving or anchoring magnetic fields for paired interactive control in a multiple robot system [11], [23], [24], [25]. On the other hand, employing aiding method [12], [26], [27], [28], such as additional field drive sources and special environmental structures, allows for individual control within a multitarget robotic system. Additional drive sources, such as light [29], sound [30], and fluid [32], are able to anchor individual millirobots in conjunction with magnetic fields to achieve paired interactive motion control in 2-D and 3-D. However, these strategies position millirobots at large intervals or employ external drives with high strength, thereby neglecting the nonlinear interactions among multiple magnetic millirobots, such as magnetic dipole-dipole, hydrodynamic, and capillary forces. When the millirobots are large and the distance is too close, the paired interactive motion is significantly disturbed by these nonlinear interindividual forces. The dynamic control of paired millirobots with accurate force interactions remains a significant challenge.

Open-loop control or linear proportional control methods are generally used to achieve fundamental behavioral interactive control among multiple millirobots, which facilitates the transition of millirobots from disorder to order, as characterized by convergence or separation. Gardi et al. [14] and Wang et al. [32] adjusted the rotation frequency of the magnetic field to control the spacing distance of magnetic multiple millirobot systems. Piñan Basualdo et al. [15] used the PI algorithm to control the rotation speed of multiple millirobots to generate flow fields to accurately control the position of passive particles. Zhang et al. [33] adjusted the local magnetic interactions of two microgrippers to facilitate position control when operating in close proximity. Salehizadeh and Diller [16], [34] proposed a dynamic oscillating magnetic field control method to realize the autonomous operation of the relative pose of two millirobots. However, as the scale decreases, both environmental factors (thermal noise and boundary effects) and the magnetic drive system (magnetic field distortion and signal lag) introduce simultaneous nonlinear disturbances [17], [26], [35], [36], [37], resulting in random deviations between the actual paired interactive motions within multiple millirobots and the intended motion. Furthermore, slight individual differences may lead to difficulty in establishing an accurate paired interactive motion model [6], [36], which is caused by the manufacturing process, including body structure (size and mass) and magnetization performance (magnetic substance content and magnetic moment direction). Consequently, to accurately control paired millirobots, conventional open-loop and linear controllers are inadequate for rectifying spacing errors arising from interindividual interactions. Hence, there is a crucial need for a nonlinear motion control method in multiple magnetic millirobot systems to enable more precise paired interactions within confined motion spaces.

In this study, we propose a paired interactive control method that enables the precise formation of two millirobots in a multiple millirobot system under identical control signals and interindividual forces. To decouple paired interactions within a multiple millirobot system, the model of paired interactions is transformed into an individual point-reaching model. Precise tracking control is provided by a nonlinear composite controller. A mapping model between the magnetic field state and the movement state of the pair is established as a feedforward controller via the nonlinear inversion control method, which enables the control system to rapidly achieve the desired state. To eliminate residual tracking errors, a model-free feedback controller is designed on the basis of the active disturbance rejection concept, which involves the estimation and elimination of generalized disturbances by an extended state observer. The control method is validated via two millirobots that precisely follow an arbitrary planar formation both in isolation and within a multiple millirobot system under identical control signals. This research provides a novel basic paired control paradigm for multiple magnetic millirobot motion guided by global stimuli in a confined space.

The rest of this article is organized as follows. Section II delves into the dynamics of multiple millirobot systems. Section III presents the controller design. Section IV validates the proposed method through experiments. Finally, Section V concludes this article.

II. Mathematical Modeling

Magnetic millirobots can stably float and move at the liquid-air interface. In the absence of any external forces or moments, these millirobots remain stationary. In our study, we employ a uniform planar rotating magnetic field $\boldsymbol{B}(f,t)$ parallel to the liquid surface (xy plane) as the driving force for magnetic millirobots. Within these fields, the millirobot is propelled by magnetic torque, executing spin motion. In the theoretical analysis, it is assumed that the magnetic moment of the magnetic millirobot and the applied magnetic field are aligned within the working space. The planar rotating magnetic field can be described by

$$\boldsymbol{B}\ (f,t) = B\left[\sin\left(2\pi f t\right)\mathbf{e}_{\boldsymbol{x}} + \cos\left(2\pi f t\right)\mathbf{e}_{\boldsymbol{y}}\right] \tag{1}$$

where B is the magnitude, f is the magnetic field rotation frequency, and $\mathbf{e}_{\boldsymbol{x}}$, and $\mathbf{e}_{\boldsymbol{y}}$ are the unit vectors of the x- and y-axes, respectively.

Individual Motion Analysis: Initially, the planar motion characteristics of a magnetic millirobot are examined. When subjected to a rotating magnetic field, the millirobot can exhibit spinning motion in alignment with the magnetic field, with its rotational axis centered on its geometric midpoint. Additionally, the applied magnetic field is uniform and lacks any magnetic field gradient, thereby resulting in negligible magnetic force. Throughout its planar movement, the millirobot experiences the influence of both magnetic torque and fluid dynamics. The planar force acting on a magnetic millirobot is illustrated in Fig. 1(a),

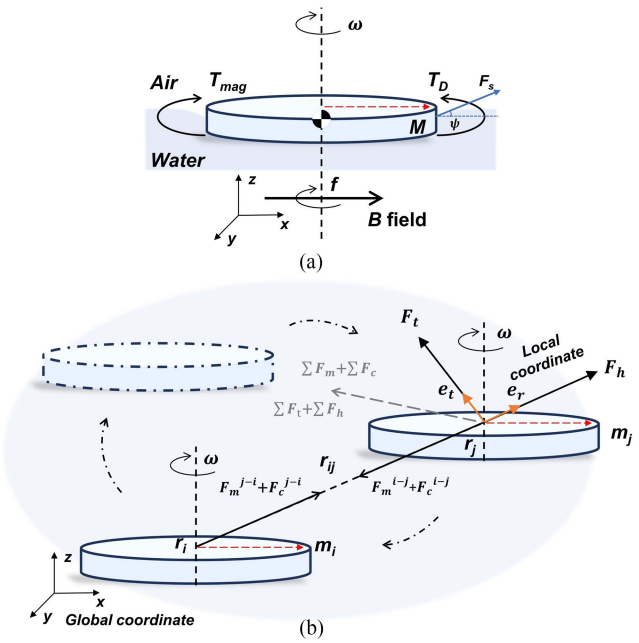

Fig. 1. Dynamic analysis of millirobots driven by a rotating magnetic field at an air-water interface. (a) Single millirobot system. (b) Paired interaction within a multiple-millirobot system.

while on the basis of torque equilibrium conditions, the dynamic relationship is expressed by the following equation:

$$\boldsymbol{T_{mag}} + \boldsymbol{T_D} = I\ddot{\boldsymbol{\theta}} \tag{2}$$

$$\boldsymbol{T_{mag}} = V\boldsymbol{M} \times \boldsymbol{B} = VMB\sin(2\pi ft - \theta) \tag{3}$$

where $\boldsymbol{T_{mag}}$ is the magnetic torque, $\boldsymbol{T_D}$ is the fluid resistance moment, I is the moment of inertia, and $\ddot{\boldsymbol{\theta}}$ is the angular acceleration of the millirobot motion. V and $\boldsymbol{M}$ are the volume and magnetization of the millirobot, respectively.

The millirobot can be approximated as a spheroid for the calculation of drag moments

$$T_D = C_R\,\dot{\boldsymbol{\theta}} = -8\pi\mu R^3\omega \tag{4}$$

where C_R is the rotational damping coefficient, μ is the fluid viscosity, R is the radius of the millirobot, and ω is the rotational speed of the millirobot.

When the magnetic millirobot rotates at a constant speed, both the millirobot and the external magnetic field rotate simultaneously, resulting in a dynamic equilibrium between the magnetic moment and the resistance moment

$$\boldsymbol{T_{mag}} + \boldsymbol{T_D} = 0. \tag{5}$$

When the magnetic millirobot fails to synchronize its rotation with the external magnetic field, the frequency of the external rotating magnetic field exceeds a certain threshold. Consequently, the critical driving magnetic field frequency for achieving the maximum angular velocity can be determined $\omega_{\text{step-out}}$, where

$$\omega = \frac{BVM\sin(2\pi ft - \theta)}{8\pi\mu R^3} \tag{6}$$

$$\text{s.t. } \omega_{\text{step-out}} = \frac{BVM}{8\pi\mu R^3}.$$

Interactive Motion Analysis: The planar motion of multiple magnetic millirobots driven by rotating magnetic fields is influenced by three primary factors, as shown in Fig. 1(b). First, a magnetic dipole-dipole force [32], [14], [16], [38] ensues when interactions between magnetic substances occur when the distance between them falls below a specific threshold. Second, a capillary force [32], [14], [39] refers to the lateral component of the liquid surface tension, which arises from the deformation of the liquid surface due to the presence of suspended magnetic millirobots at the air-water interface. When averaged over a complete rotation of the millirobot, the magnetic dipole force is characterized by mutual attraction. Whereas the capillary force is characterized by mutual repulsion or mutual attraction, depending on the state of the millirobots [39]. Third, a hydrodynamic force [32], [16], [14], [40], is produced when magnetic millirobots rotate and interact with the liquid, and they also encounter the flow field produced by other millirobots. This hydrodynamic force is contingent upon the instantaneous angular velocity of the millirobots and consistently exhibits a repulsive nature. When attractive and repulsive forces interact in equilibrium, the millirobots maintain a finite steady-state distance as they rotate around their respective centers.

The magnetic force $\boldsymbol{F_m}^{i-j}$ of millirobot i acting on millirobot j can be expressed as [32], [16]

$$\boldsymbol{F_m}^{i-j} = \frac{3\mu_0}{4\pi {r_{ij}}^4} Q \tag{7}$$

$$\text{s.t. } Q = [\boldsymbol{r_{ij}}(\boldsymbol{m_i}\cdot\boldsymbol{m_j}) + \boldsymbol{m_i}(\boldsymbol{r_{ij}}\cdot\boldsymbol{m_j}) + \boldsymbol{m_j}(\boldsymbol{r_{ij}}\cdot\boldsymbol{m_i}) - 5\boldsymbol{r_{ij}}(\boldsymbol{r_{ij}}\cdot\boldsymbol{m_i})(\boldsymbol{r_{ij}}\cdot\boldsymbol{m_i})]$$

where μ_0 is the vacuum permeability, which is the same as the permeability of water and air. $\boldsymbol{m_i}$ and $\boldsymbol{m_j}$ are the magnetic moments of the two magnetic millirobots. $\boldsymbol{r_{ij}}$ is the vector that moves from millirobot i to millirobot j.

The magnetic torque $\boldsymbol{T_m}^{i-j}$ of millirobot i acting on millirobot j is expressed as follows:

$$\boldsymbol{T_m}^{i-j} = \frac{\mu_0}{4\pi {r_{ij}}^3}\left[3(\boldsymbol{r_{ij}}\cdot\boldsymbol{m_i})(\boldsymbol{m_j}\times\boldsymbol{r_{ij}}) + (\boldsymbol{m_i}\times\boldsymbol{m_j})\right]. \tag{8}$$

Inspired by [39], the asymptotic expression for calculating the transverse capillary force between millirobots i and j is $\boldsymbol{F_c}^{i-j}$ and is expressed as follows:

$$\boldsymbol{F_c}^{i-j} = -2\pi\sigma q K_i \sin\psi_i K_j \sin\psi_j F(q|r_{ij}|)\left(1 + o\left(q^2 {R_j}^2\right)\right) \tag{9}$$

where $\boldsymbol{F_c}^{j}$ is the capillary force on millirobot j, σ is the surface tension coefficient of the liquid, and $F(\cdot)$ is a first-order modified Bessel function. K_i, K_j, and q are constants, for which $q^{-1} = 2.7\,\text{mm}$ for liquid water. ψ is the deformation angle of the liquid surface caused by the millirobot. When $\sin\psi_i\sin\psi_j > 0$, the capillary force is the attractive force. When $\sin\psi_i\sin\psi_j < 0$, the capillary force is repulsive.

The hydrodynamic force generated by the superposition of the flow field generated by the millirobot j and the self-generated rotating flow field in the millirobot i can be calculated as

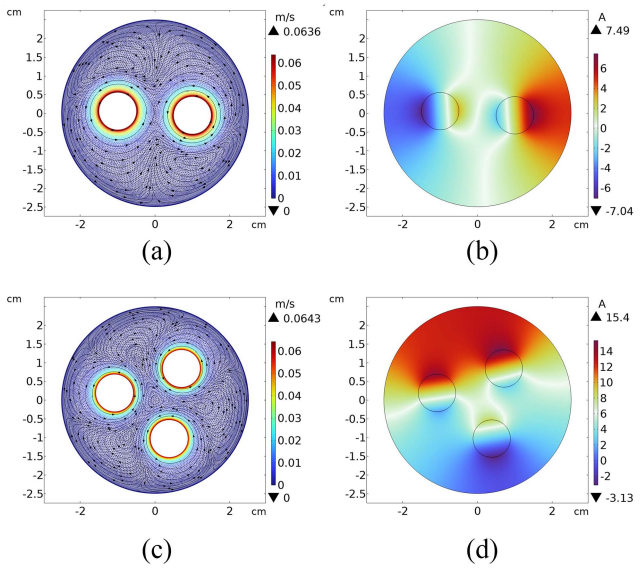

Fig. 2. Simulation results of magnetic millirobots in a rotating magnetic field at a confined air-water interface. (a) and (c) Fluid flow velocity diagrams affected by the rotating millirobots. (b) and (d) Schematic diagram illustrating the magnetic scalar potential associated with the magnetization of the millirobots.

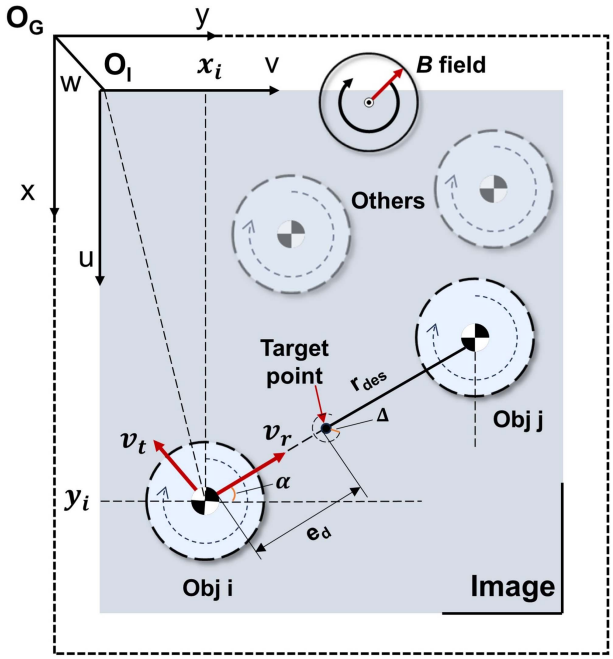

Fig. 3. Paired interactive kinematics model of a multiple-millirobot system.

follows [40]:

$$\boldsymbol{F_{hr}} = c_h\ \rho\mu\omega^2 \frac{{R_j}^4 {R_i}^3}{|\boldsymbol{r_{ij}}|^3}\boldsymbol{e_r} \tag{10}$$

$$\boldsymbol{F_{ht}} = c_t\ \rho\mu\omega \frac{{R_j}^3}{|\boldsymbol{r_{ij}}|^2}\boldsymbol{e_t} \tag{11}$$

where $c_{h,t}$ is a constant, ρ is the density of water, μ is the viscosity of water, ω is the magnitude of the angular velocity of the millirobot, and $R_{i,j}$ is the radius of the millirobot. $\boldsymbol{e_r}$ and $\boldsymbol{e_t}$ are the unit vectors in the $\boldsymbol{r_{ij}}$ direction and perpendicular to $\boldsymbol{r_{ij}}$.

Since the capillary force is much smaller than the magnetic force, it has often been ignored in previous studies. In this study, we model it as a part of lump perturbation $\boldsymbol{\delta}$. Based on the above interaction between gravitational and repulsive forces, the dynamics of the millirobot i can be further expressed as follows:

$$\boldsymbol{\delta} + \sum_{j\neq i} \boldsymbol{F_m}^{\boldsymbol{j-i}} + \sum_{j\neq i} \boldsymbol{F_h}^{\boldsymbol{i}} = m\ddot{\boldsymbol{r}}. \tag{12}$$

Hence, the movement of the millirobot is controlled by modifying the rotation speed by adjusting the frequency of the rotating magnetic field. Owing to the small size of the millirobot, the Reynolds number R is low, and the viscous force is dominant. When the millirobot moves at a steady and uniform speed, the fluid force, magnetic force, and capillary force balance each other. The finite element simulation results of the flow field generated by the magnetic millirobots are shown in Fig. 2(a) and (c). In addition, the simulation results of the magnetic interactions between multiple magnetic millirobots are shown in Fig. 2(b) and (d). The simulation was accomplished by using COMSOL Multiphysics software (COMSOL Inc., Stockholm, Sweden). The fluid medium is deionized water, which is set to an incompressible and laminar flow. The millirobot moves passively when driven by a rotating magnetic field. More detailed simulation settings are provided in the *Supplementary Information S1*.

III. Controller Design

The system is controlled by a rotating magnetic field, with the magnetic field rotation frequency serving as the single control variable to adjust the rotation speed of the millirobots. This alteration in speed modifies the fluid resistance, facilitating position control. The transverse component of the hydrodynamic force controls the millirobot spacing, whereas the radial component characterizes the circular motion of the millirobots. Note that control objects are restricted to millirobots capable of achieving stable rotational motion on the liquid surface. Furthermore, spacing boundary constraints $r_{\min} < r < r_{\max}$: The interaction force (magnetic and fluid interactions) between the magnetic millirobots decreases rapidly with increasing distance. When the distance exceeds a certain threshold, the interaction force is insignificant compared with the driving force, which can be ignored. Conversely, when millirobots come too close to each other, a stable separation cannot be maintained, as the repulsive forces are insufficient to counteract the attractive forces.

Controlling the spacing between millirobots can be conceptualized as a point-reaching problem involving a single millirobot, representing an iterative process (see Fig. 3). After each iteration, the millirobot center moves closer to the target point (x_d, y_d) within a specified tolerance threshold

$$|\boldsymbol{r_{ij}} - \boldsymbol{r_{des}}| = \sqrt{(y_d - y_i)^2 + (x_d - x_i)^2} < |\Delta| \tag{13}$$

where $|\Delta|$ is a small real constant.

In the context of controlling the distance $\boldsymbol{r_{ij}}$ between any millirobot $\boldsymbol{P_i}(x_i, y_i)$ and millirobot $\boldsymbol{P_j}(x_j, y_j)$, the target point is denoted as $\boldsymbol{P}\ (x_p, y_p)$, whereas the discrepancy in distance is defined as the distance error $\boldsymbol{e_d} = \boldsymbol{P_i}\ - \boldsymbol{P}$. The velocity of the millirobot i is broken down into the vector $\boldsymbol{v_r}$, which represents the connection direction with the target millirobot j, and the vector $\boldsymbol{v_t}$, which indicates the tangential direction of the vector $\boldsymbol{v_r}$. The desired distance between the target millirobots is denoted as r_{des}, as depicted in Fig. 3. The kinematic geometric relationship is as follows:

$$\frac{|y_d - y_j|}{|x_d - x_j|} = \frac{|y_j - y_i|}{|x_j - x_i|} \tag{14}$$

$$\frac{|y_d - y_j|}{|y_j - y_j|} = \frac{|\boldsymbol{e_d}|}{|\boldsymbol{r_{ij}}|}\,. \tag{15}$$

To achieve precise control of millirobot motion, it is imperative to mitigate uncertain disturbances stemming from the environment and the magnetic control system, including factors such as capillary forces, wall effects, hysteresis, and magnetic field saturation. Additionally, the uncertainties in the motion model of millirobots can lead to deviations in motion control, necessitating compensation within the control framework. Active disturbance rejection control introduces the generalized disturbance, which includes internal dynamics and external disturbances, to the design control law. A nonholonomic car-like robot single input single output (SISO) motion model can be used to control the motion of any single millirobot in a multiple millirobot system. The augmented state space form is presented as follows:

$$\begin{cases} \dot{\boldsymbol{x}} = \boldsymbol{A} \cdot \boldsymbol{x} + \boldsymbol{B} \cdot u + \boldsymbol{E}h \\ y = \boldsymbol{C} \cdot \boldsymbol{x} \end{cases}$$

$$s.t.\ \boldsymbol{A} = \begin{bmatrix} 0 & 1 & 0 \\ 0 & 0 & 1 \\ 0 & 0 & 0 \end{bmatrix},\ \boldsymbol{B} = \begin{bmatrix} 0 \\ b \\ 0 \end{bmatrix},\ \boldsymbol{C} = \begin{bmatrix} 1 & 0 & 0 \end{bmatrix},\ \boldsymbol{E} = \begin{bmatrix} 0 \\ 0 \\ 1 \end{bmatrix} \tag{16}$$

where $\boldsymbol{x} = [\boldsymbol{x}_1 \quad \boldsymbol{x}_2 \quad \boldsymbol{x}_3]^T$ denotes the millirobot position, velocity, and generalized disturbance. u is the input for the controlled system, which is the rotation speed ω of the millirobot. The physical meaning of y is the distance between millirobots, and h is the differentiation of the generalized disturbance.

The linear state observer is presented as follows:

$$\begin{cases} \dot{\boldsymbol{z}} = \boldsymbol{A} \cdot \boldsymbol{z} + \boldsymbol{B} \cdot u + \boldsymbol{L}\,(y - \hat{y}) \\ \hat{y} = \boldsymbol{C} \cdot \boldsymbol{z} \end{cases} \tag{17}$$

where $\boldsymbol{L} = [\ L_1 \quad L_2 \quad L_3\ ]$ denotes the observer gains. $\boldsymbol{z}$ is the estimate of $\boldsymbol{x}$.

The control law is designed as

$$u\ = (-|\boldsymbol{z}_3| + u_0)\ /b \tag{18}$$

$$u_0 = k_p\ (|\boldsymbol{p} - \boldsymbol{z}_1|) - k_d\,|\boldsymbol{z}_2| \tag{19}$$

where $\boldsymbol{z}_3$ is the estimation of the generalized disturbance and where k_p and k_d are control gains.

The tracking error in the linear state observer is presented as follows:

$$\boldsymbol{e} = \boldsymbol{x} - \boldsymbol{z} \tag{20}$$

$$\dot{\boldsymbol{e}} = \boldsymbol{A_e}\,\boldsymbol{e} + \boldsymbol{D} \tag{21}$$

$$\text{s.t.}\ \ \boldsymbol{A_e} = \begin{bmatrix} -L_1 & 1 & 0 \\ -L_3 & 0 & 1 \\ -L_3 & 0 & 0 \end{bmatrix},\ \boldsymbol{D} = \boldsymbol{E}h.$$

Assuming that the observer gains $\boldsymbol{L}$ are selected appropriately, $\boldsymbol{A_e}$ is Hurwitz. In addition, we assume that the derivatives of the generalized disturbance in $\boldsymbol{D}$ are bounded. Theoretically, the designed observer is convergent, and the estimation error is bounded [35], [41].

To increase the control speed, mitigate the output overshoot, and minimize the output jitter resulting from significant errors, we devised a feedforward controller that leverages a data-driven approach. In an ideal scenario, the perturbation model enables us to calculate and offset deviations induced by system disturbances. However, practical engineering applications pose challenges in accurately determining system parameters and environmental variables, hindering precise error compensation through theoretical calculations. The data-driven methodology effectively addresses this issue by enabling direct mapping of the input–output data relationships within the system via machine learning techniques, bypassing the need for meticulous mathematical analysis of the system [6], [36].

In this work, the distance data d_t and the driving magnetic field frequency data f_t of both the controlled millirobot and the target millirobot in an L-group multiple millirobot system are sampled. On the basis of these data samples, a mapping model F is established as follows:

$$\hat{d}_{t+1} = F\,(q_t, f_t) \tag{22}$$

$$q_t\ = (d_t, \ldots, d_{t-n+1}, f_t, \ldots, f_{t-n+1}) \tag{23}$$

where $\hat{d}$ is the mapping model output.

The reference structure of the mapping model is designed as polynomial function

$$F\,(q_t, f_t) = \sum_{i=1}^{N} m_i g_i\,(q_t, f_t) \tag{24}$$

where g_i is a polynomial function and where m_i represents parameters. The parameter vector m_i can be identified through sqrt-LASSO regression.

To prevent situations where the mapping model fails to calculate the corresponding analytical frequency value for a given expected distance d^*, such that the distance output matches the anticipated value ($F(q_t, f_t) \nexists d^*$), the feedforward control output u_f is derived through the online inversion of this mapping model

$$u_f = \text{argmin}\frac{1}{\rho}(d^* - F\,(q_t, f))^2 \tag{25}$$

$$\text{s.t.}\ \ f_{\min} < f < f_{\max}$$

where $\rho = \|(d_L, \ldots, d_0)\|_2^2\ /L$.

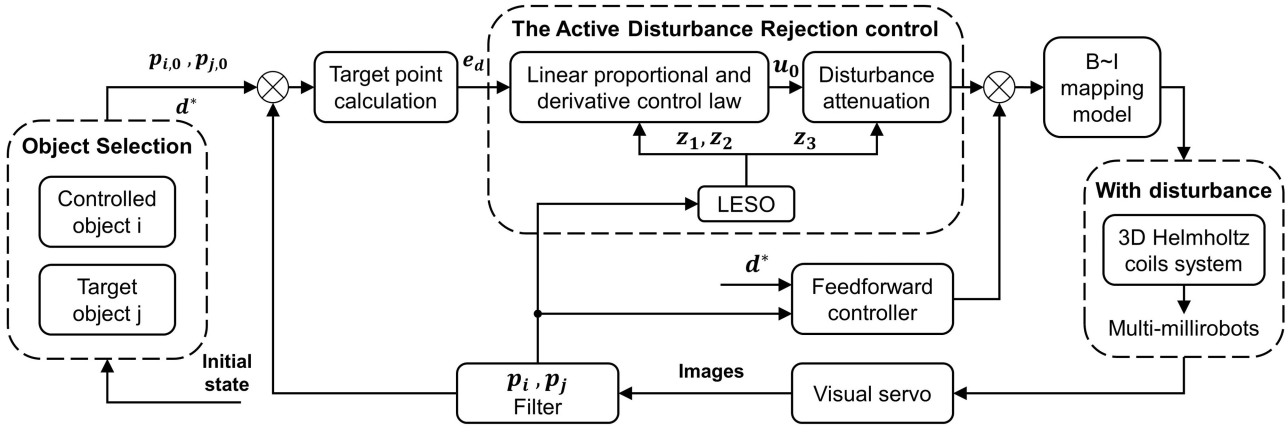

Fig. 4. Paired interactive motion control block diagram.

TABLE I
DISTANCE PREDICTION ERROR (MM)

Error	DS 1	DS 2	DS 3	DS 4
Rms	0.426	0.399	0.447	0.408
Max	-1.151	-1.013	-1.201	1.114
Min	0.015	0.033	-0.024	-0.011

To verify the accuracy of the model, we performed four sets of tests. Table I shows the prediction error results of the mapping model. Because the feedback controller eliminates the residual error under feedforward control, the feedforward controller does not need to be extremely accurate. Moreover, the original intention of the feedforward controller is to avoid overshoot oscillation caused by large initial errors. Hence, the composite controller developed in this study comprises a nonlinear mapping model controller and an active disturbance rejection feedback controller, as illustrated in Fig. 4. Note that the selection of the controlled object is chosen arbitrarily by the user on the basis of the first frame image obtained at the beginning of the program, the details of which are shown in *Supplementary Information S2*.

IV. EXPERIMENTAL RESULTS

A. Experimental Setup

The magnetic field generation device utilized in this study is a self-developed three-position Helmholtz coil system capable of producing a magnetic field with a peak intensity of 15 mT within the central region of the operational space (see Fig. 5). The coil system can generate a homogeneous magnetic field within a spherical region measuring 100 mm in diameter, and the nonuniformity (the percentage change in the magnetic field value at any point in the workspace relative to the magnetic field value at the center point) is less than 1. Any motion inaccuracies arising from magnetic field nonuniformity are rectified through the implementation of a control algorithm. Real-time current control instructions are produced by the upper computer software, whereas the lower computer provides pulse-width

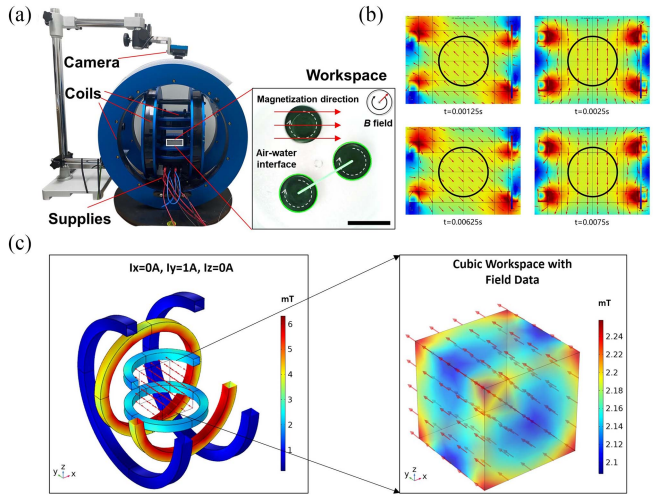

Fig. 5. Schematic diagram of electromagnetic drive system. (a) Three-dimensional Helmholtz coil system. (b) Simulation results of rotating magnetic field. (c) Simulation results of magnetic field distribution in workspace.

modulation (PWM) signals to regulate the three motor drives (Maxon ESCON 70/10), thereby generating the current for the input coil. The movement of the millirobots was continuously monitored in real time by an industrial camera (Olympus DP21). The following formula is derived in accordance with the principle of linear superposition:

$$\boldsymbol{B}\ (P) = \sum_{i=1}^{n} \tilde{\boldsymbol{B}}_{\boldsymbol{i}}\,(P)\, I_i\ = \tilde{B}\ (P)\, \boldsymbol{I} \tag{26}$$

where n indicates the number of coils, $\tilde{\boldsymbol{B}}_{\boldsymbol{i}}(P) \in \mathbb{R}^{3\times 1}$ is a matrix that depends on the measuring point P, and $\boldsymbol{I} \in \mathbb{R}^{3\times 1}$ denotes the control current in each coil.

The millirobot is constructed by demolding technology. A container measuring 10 mm in diameter and 0.5 mm in height was filled with a precuring solution of ferric tetroxide–polydimethylsiloxane (PDMS) (1:1) and subsequently heated at a constant temperature for curing, resulting in the release of the robot. The millirobot is magnetized within a uniform magnetic

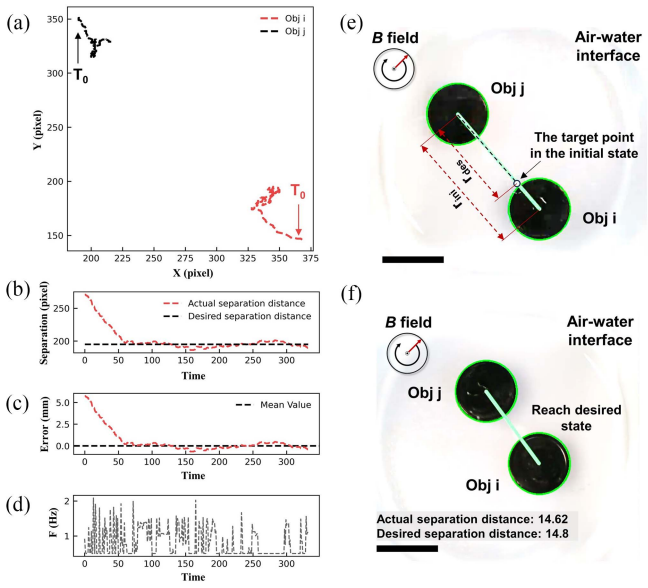

Fig. 6. Step signal Test I for two millirobots. This is the case when the two millirobots are far apart in the initial state. (a) Real-time motion trajectory data graph. (b) Spacing variation data graph. (c) Control error. (d) Control signal. (e) and (f) Control process image sequence. The scale bar is 10 mm.

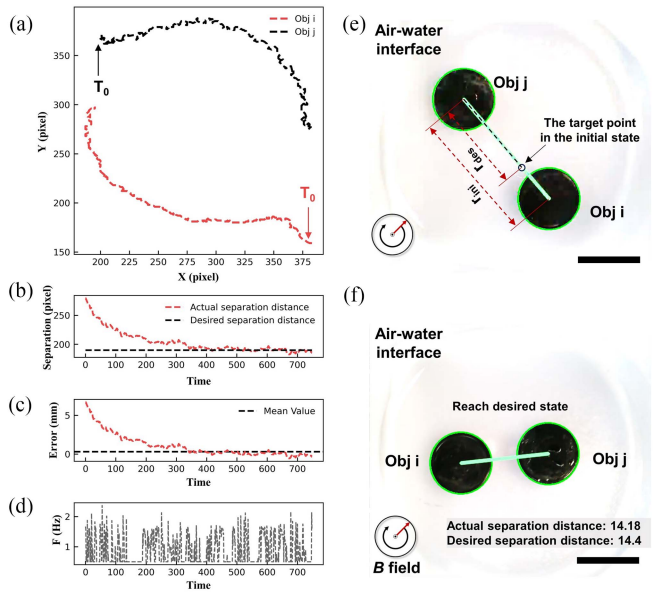

Fig. 7. Step signal Test II for two millirobots. Circular motion occurs when the distance between the two millirobots is not far from the expected value. (a) Real-time motion trajectory data graph. (b) Spacing variation data graph. (c) Control error. (d) Control signal. (e) and (f) Control process image sequence. The scale bar is 10 mm.

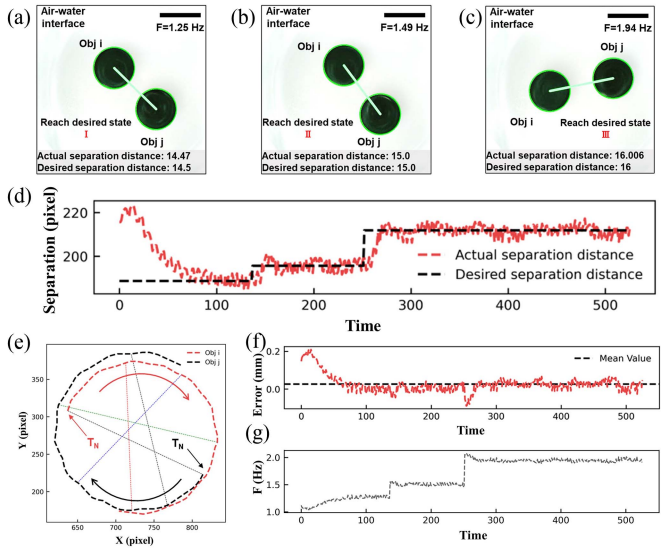

Fig. 8. Continuous step signal excitation experimental results of two millirobots. (a)–(c) Two millirobots stably follow three desired distances. (a) Desired State I. (b) Desired State II. (c) Desired State III. (d) Spacing variation data graph. (e) Trajectory data graph during transition from State II to State III. Five moments are selected to connect the center of mass of the two millirobots. (f) Control error. (g) Control signal. The scale bar is 10 mm.

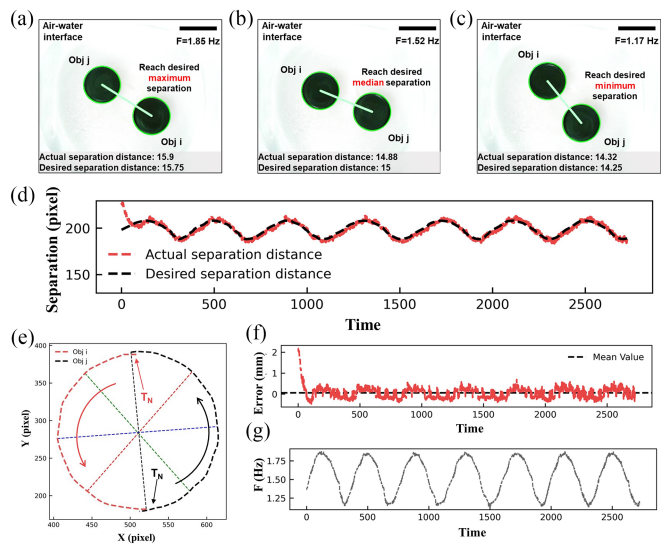

Fig. 9. Sinusoidal signal excitation experimental results of two millirobots. (a)–(c) Two millirobots stably follow three desired distances. (a) Desired maximum separation. (b) Desired median separation. (c) Desired maximum separation. (d) Spacing variation data graph. (e) Trajectory data graph during transition from the peak of the sine wave. Four moments are selected to connect the center of mass of the two millirobots. (f) Control error. (g) Control signal. The scale bar is 10 mm.

field with an intensity of 1 T, and the direction of magnetization is indicated in Fig. 5(a).

B. Paired Interactive Control

The experimental demonstration of paired interactive control is conducted in a culture vessel placed at the center of the coil system workspace and filled with deionized water. The millirobots float on the liquid surface within this vessel. Real-time feedback is provided via a top camera that captures images at 30 frames per second. The motion information of the millirobot is processed via the standard OpenCV library. The millirobots under control conditions are identified by green rings. The

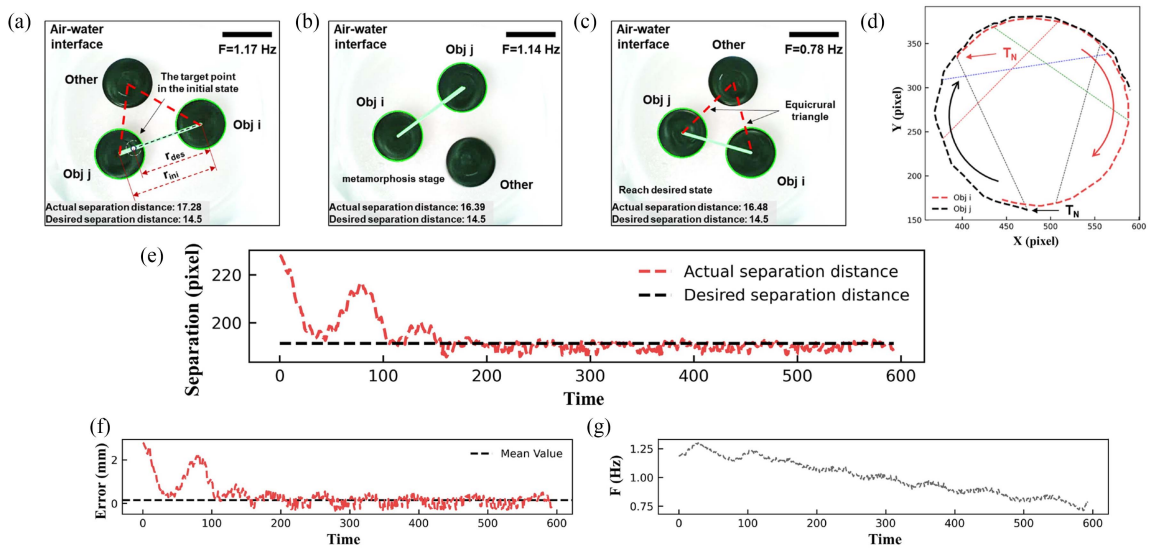

Fig. 10. Step signal excitation for two millirobots within a multiple millirobot system. (a)–(c) There are three stages of adjusting the spacing: initial state, adjustment state, and steady state. (d) Intercepted trajectory data graph. Five moments are selected to connect the center of mass of the two millirobots. (e) Spacing variation data graph. (f) Control error. (g) Control signal. The scale bar is 10 mm.

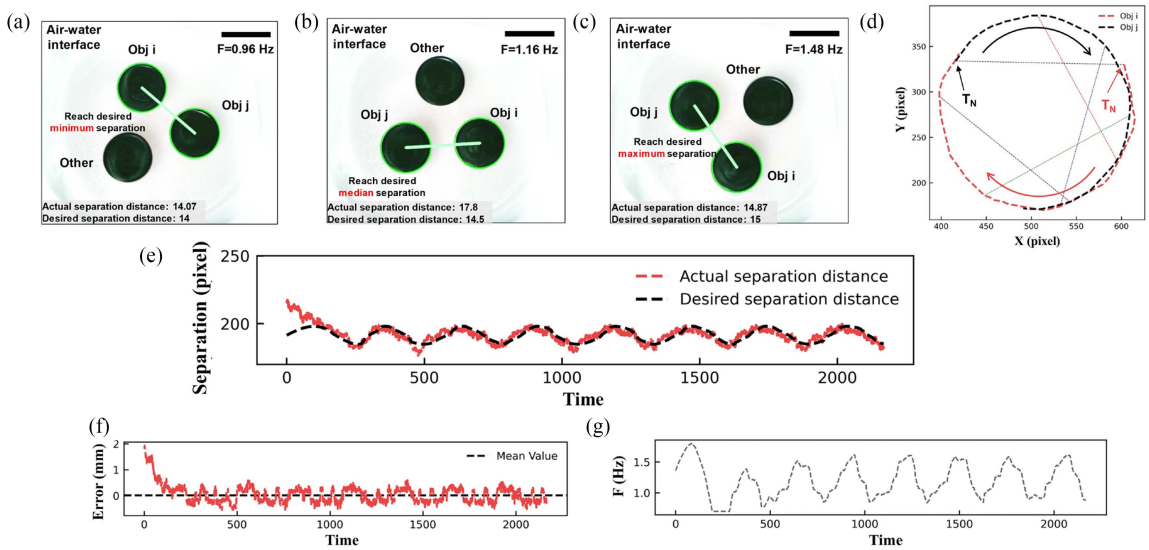

Fig. 11. Sinusoidal signal excitation for two millirobots within a multiple millirobot system. (a)–(c) There are three stages of adjusting the spacing: sinusoidal troughs, boundaries, and crests. (d) Intercepted trajectory data graph. Five moments are selected to connect the center of mass of the two millirobots. (e) Spacing variation data graph. (f) Control error. (g) Control signal. The scale bar is 10 mm.

distance between these controlled machines is expressed by the line connecting the centers of the two circles.

The paired interactive control performance of the two millirobots is initially tested under step signal excitation. When subjected to step signal excitation, the response of the rotating two millirobots manifests in three scenarios: if the current distance significantly deviates from the desired distance, the two millirobots will rapidly converge akin to the swift attraction observed between two magnets, as shown in Fig. 6(a); if the current distance closely aligns with the expected distance, the two millirobots will adjust their distance while executing circular motion, as illustrated in Fig. 7(a); if the current distance reaches the desired distance, the two millirobots will initiate a stable circular motion while self-rotating, with the diameter of the circular trajectory equaling the distance between the two millirobots, as shown in *Supplementary Video S1*. This behavior mirrors the mutual orbit observed in binary stars of equal mass. Figs. 6 and 7 show the actual motion state image, spacing change data, control error data, and control signal data. The control method proposed in this study results in a steady-state distance error of less than 0.21 mm (approximately 2.1% of the body length of a single millirobot) under step signal excitation, which is less than one-third of the error observed with the proportion integration differentiation (PID) controller, as shown in Table II.

TABLE II
CONTROL ERROR OF DIFFERENT CONTROLLERS (MM)

Experimental type	Error type	Feedforward control	PID control	Our method
Two millirobots in isolation under step signal excitation	Rms	0.85	0.66	**0.21**
	Max	1.7	2.12	**0.03**
	Min	0.16	0.12	0.001
Two millirobots in isolation under stairstep signal excitation	Rms	0.84	0.88	**0.29**
	Max	2.34	2.39	**0.82**
	Min	0.1	0.11	0.1
Two millirobots in isolation under sinusoidal signal excitation	Rms	0.66	0.75	**0.22**
	Max	3.09	2.81	**0.69**
	Min	0.1	0.1	0.1
Two millirobots within a multiple millirobot system under step signal excitation	Rms	0.76	0.38	**0.25**
	Max	1.99	1.59	**0.6**
	Min	0.1	0.1	0.1
Two millirobots within a multiple millirobot system under sinusoidal signal excitation	Rms	0.62	0.39	**0.25**
	Max	2.35	1.58	**0.65**
	Min	0.1	0.1	0.1

A stairstep signal excitation experiment is conducted, with three distinct desired distance signals. Fig. 8 clearly shows that the adjustment time is correlated with the variance between the current spacing and the desired spacing. In Fig. 8(e), the motion trajectories of the two millirobots depict a spin transition from the desired Distance I to the Desired distance II, with connections established between the spacings of five different moments. The distance variation, control error and control signal are shown in Fig. 8(d), (f), and (g). Finally, two millirobots are stimulated by continuously varying sinusoidal signals. As depicted in Fig. 9(b), the spacing between the spinning machines accurately adheres to the predetermined sinusoidal variation pattern. Fig. 9(e) displays the motion trajectory of the two millirobots spinning under the excitation of a sinusoidal wave crest signal, with intervals connecting 4 specific moments. The control error and control signal are shown in Fig. 9(d), (f), and (g). With the control technique proposed in this research, the steady-state errors remain below 2.2% of a single robot body length, demonstrating favorable control efficacy. The tracking error comparison results of the above experiments under the action of different controllers are shown in Table II, where we analyze three scenarios involving the utilization of a feedforward controller only, a PID controller, and the controller introduced in this study.

We also tested paired interactive control when the controlled system included other spinning millirobots. Excitation signals include step signals and sinusoidal signals. The experimental outcomes of paired interactions are illustrated in Figs. 10 and 11(*Supplementary Video S2*), which show images of the experimental process, trajectory plots demonstrating stable spacing, spacing variation data, control error data, and control signal data. Under step and sinusoidal signal excitation, the root mean square (rms) errors are both 0.25 mm. Within the multiple millirobot system, the proposed paired interactive control method enables precise tracking control. The tracking error comparison results of the above experiments under the action of different controllers are shown in Table II. When three millirobots are present in the system, stable paired interactions can lead to the formation of an isosceles triangle configuration, as illustrated in Fig. S3. Under step signal excitation, if the distance between the two controlled millirobots stabilizes at a steady state, the unselected millirobot can maintain a constant spacing with each of the two millirobots.

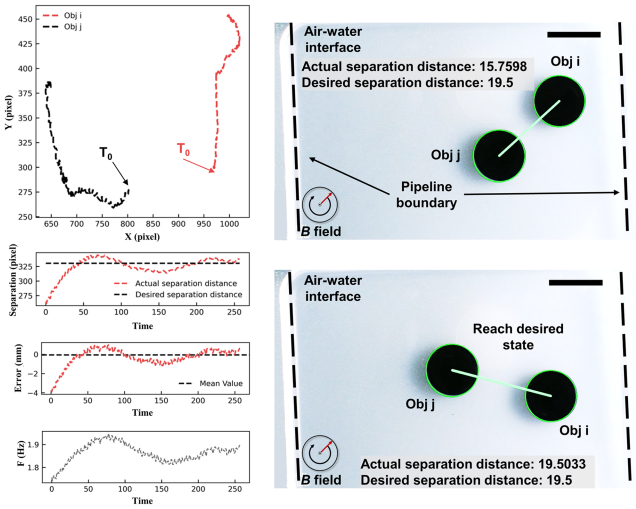

Fig. 12. Step signal test for two millirobots in a pipeline environment. (a) Real-time motion trajectory data graph. (b) Spacing variation data graph. (c) Control error. (d) Control signal. (e)–(f) Control process image sequence. The scale bar is 10 mm.

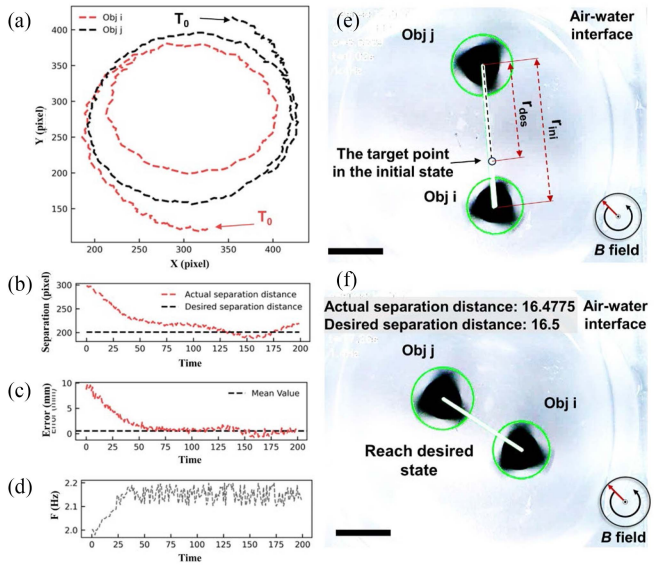

Fig. 13. Step signal test for two millirobots (triangle). (a) Real-time motion trajectory data graph. (b) Spacing variation data graph. (c) Control error. (d) Control signal. (e) and (f) Control process image sequence. The scale bar is 10 mm.

To further verify the adaptability of the proposed method, we conducted interaction experiments with millirobots in a pipeline environment (see Fig. 12). Additionally, we altered the shape of a single or two millirobots to triangle for an interactive experiment (see Figs. 13 and 14). The spacing errors converge asymptotically to near zero. The results are similar to those of *Tests I* and *II* under step signals.

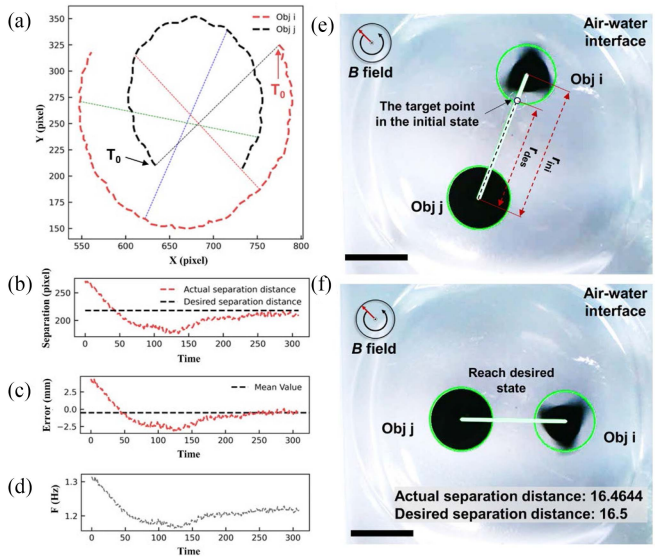

Fig. 14. Step signal test for two millirobots (triangle and circle). (a) Trajectory data graph of steady state. Four moments are selected to connect the center of mass of the two millirobots. (b) Spacing variation data graph. (c) Control error. (d) Control signal. (e) and (f) Control process image sequence. The scale bar is 10 mm.

V. Conclusion

In this study, within a multiple millirobot system, the paired interactive control problem is decoupled into individual millirobot point-reaching problems, and an interactive control scheme for two millirobots is proposed that enables precise formation under identical control signals and interindividual forces. By mapping the magnetic field actuation and the paired movement as a nonlinear inversion controller, the error between the initial state and the expected state is greatly reduced. Then, the tracking error can be eliminated by an observer-based disturbance rejection controller. Comparative experimental results demonstrate a significant improvement in addressing the paired interaction problem of multiple millirobot systems achieved by the proposed method compared to the conventional method.

Because, we model the millirobot as a particle, even though the millirobot changes shape, as long as the motion law of the millirobot is consistent or similar, the method is effective for objects with different geometric shapes. When the millirobot shape is not uniform, our method can still achieve accurate paired interactive control of the chosen pair. However, owing to the nonuniform structure of the system, the spacing between noncontrolled millirobots may be random. Despite this randomness, the overall system will remain stable.

To achieve comprehensive formation control in a multimillirobot system, included angle control is also essential. An effective approach is to adjust the orientation of paired millirobots using periodic directional rotation magnetic fields (see *Supplementary Information S4*). However, the common magnetic field control signals induce strong coupling in the output signals of the multimillirobot system. Simultaneously controlling a pairwise separation and an included angle in a multimillirobot system need to decouple the magnetic field rotation frequency and direction. A simple feedforward decoupling method is shown in *Supplementary Information S4*.

For practical applications, it is necessary to further investigate multimillirobot system position control. In future work, we will build on the paired interactive control established in this study by introducing additional control signals (e.g., gradient magnetic fields) to enhance simultaneous position control.

References

[1] Q. Wang et al., "Tracking and navigation of a microswarm under laser speckle contrast imaging for targeted delivery," *Sci. Robot.*, vol. 9, 2024, Art. no. eadh1978.
[2] X. Liu et al., "Magnetic soft microfiberbots for robotic embolization," *Sci. Robot.*, vol. 9, 2024, Art. no. eadh2479.
[3] Z. Chen et al., "A magnetic multi-layer soft robot for on-demand targeted adhesion," *Nat. Commun.*, vol. 15, no. 1, 2024, Art. no. 644.
[4] C. Wang et al., "In situ sensing physiological properties of biological tissues using wireless miniature soft robots," *Sci. Adv.*, vol. 9, 2023, Art. no. eadg3988.
[5] S. Pane et al., "Ultrasound acoustic phase analysis enables robotic visual-servoing of magnetic microrobots," *IEEE Trans. Robot.*, vol. 38, no. 3, pp. 1571–1582, Jun. 2022.
[6] S. Xu, T. Xu, D. Li, C. Yang, C. Huang, and X. Wu, "A robot motion learning method using broad learning system verified by small-scale fish-like robot," *IEEE Trans. Cybern.*, vol. 53, no. 9, pp. 6053–6065, Sep. 2023.
[7] M. M. Micheal et al., "2D magnetic actuation and localization of a surface milli-roller in low Reynolds numbers," *IEEE Robot. Autom. Lett.*, vol. 7, no. 2, pp. 3874–3881, Apr. 2022.
[8] L. Yang et al., "An on-wall-rotating strategy for effective upstream motion of untethered millirobot: Principle, design, and demonstration," *IEEE Trans. Robot.*, vol. 39, no. 3, pp. 2419–2428, Jun. 2023.
[9] C. Huang et al., "Multimodal locomotion and cargo transportation of magnetically actuated quadruped soft microrobots," *Cyborg Bionic Syst.*, vol. 2022, Jan. 2022, Art. no. 4.
[10] J. Lu et al., "Robust control strategy of gradient magnetic drive for microrobots based on extended state observer," *Cyborg Bionic Syst.*, vol. 2022, 2022, Art. no. 9835014.
[11] F. Ongaro et al., "Design of an electromagnetic setup for independent three-dimensional control of pairs of identical and nonidentical microrobots," *IEEE Trans. Robot.*, vol. 35, no. 1, pp. 174–183, Feb. 2019.
[12] A. Bhattacharjee et al., "Magnetically controlled modular cubes with reconfigurable self-assembly and disassembly," *IEEE Trans. Robot.*, vol. 38, no. 3, pp. 1793–1805, Jun. 2022.
[13] Y. Liu et al., "Automatic navigation of microswarms for dynamic obstacle avoidance," *IEEE Trans. Robot.*, vol. 39, no. 4, pp. 2770–2785, Aug. 2023.
[14] G. Gardi et al., "Microrobot collectives with reconfigurable morphologies, behaviors, and functions," *Nat. Commun.*, vol. 13, no. 1, 2022, Art. no. 2239.
[15] F. N. Piñan Basualdo et al., "Control and transport of passive particles using self-organized spinning micro-disks," *IEEE Robot. Autom. Lett.*, vol. 7, no. 2, pp. 2156–2161, Apr. 2022.
[16] M. Salehizadeh and E. Diller, "Three-dimensional independent control of multiple magnetic microrobots via inter-agent forces," *Int. J. Robot. Res.*, vol. 39, no. 12, pp. 1377–1396, 2020.
[17] T. Xu, C. Huang, and Z. Lai, "Independent control strategy of multiple magnetic flexible millirobots for position control and path following," *IEEE Trans. Robot.*, vol. 38, no. 5, pp. 2875–2887, Oct. 2022.
[18] C. Huang, T. Xu, and X. Wu, "Leader–follower formation control of magnetically actuated millirobots for automatic navigation," *IEEE/ASME Trans. Mechatron.*, vol. 29, no. 2, pp. 1272–1282, Apr. 2024.
[19] M. Wang et al., "Selective and independent control of microrobots in a magnetic field: A review," *Engineering*, vol. 24, pp. 21–38, May 2023.
[20] S. Floyd et al., "Control methodologies for a heterogeneous group of untethered magnetic micro-robots," *Int. J. Robot. Res.*, vol. 30, no. 13, pp. 1553–1565, 2011.
[21] E. Diller et al., "Control of multiple heterogeneous magnetic microrobots in two dimensions on nonspecialized surfaces," *IEEE Trans. Robot.*, vol. 28, no. 1, pp. 172–182, Feb. 2012.

[22] E. Diller, J. Giltinan, and M. Sitti, "Independent control of multiple magnetic microrobots in three dimensions," *Int. J. Robot. Res.*, vol. 32, no. 5, pp. 614–631, 2013.
[23] G. Cui et al., "Novel coil array design and modeling for independent control of multiple magnetic microrobots," *IEEE Trans. Ind. Electron.*, vol. 70, no. 10, pp. 10302–10311, Oct. 2023.
[24] B. V. Johnson et al., "Local magnetic field design and characterization for independent closed-loop control of multiple mobile microrobots," *IEEE/ASME Trans. Mechatron.*, vol. 25, no. 2, pp. 526–534, Apr. 2020.
[25] Y. Kantaros et al., "Control of magnetic microrobot teams for temporal micromanipulation tasks," *IEEE Trans. Robot.*, vol. 34, no. 6, pp. 1472–1489, Dec. 2018.
[26] Y. Lu et al., "Closed-loop control of magnetic modular cubes for 2D self-assembly," *IEEE Robot. Autom. Lett.*, vol. 8, no. 9, pp. 5998–6005, Sep. 2023.
[27] M. Sun et al., "Multiple magneto-optical microrobotic collectives with selective control in three dimensions under water," *Small*, vol. 20, 2024, Art. no. 2310769.
[28] F. Ji et al., "Light-driven hovering of a magnetic microswarm in fluid," *ACS Nano*, vol. 14, no. 6, pp. 6990–6998, 2020.
[29] Z. Chen and Y. Zheng, "Persistent and responsive collective motion with adaptive time delay," *Sci. Adv.*, vol. 10, no. 14, 2024, Art. no. eadk3914.
[30] N. Mahkam et al., "Acoustic streaming-induced multimodal locomotion of bubble-based microrobots," *Adv. Sci.*, vol. 10, no. 35, 2023, Art. no. 2304233.
[31] F. N. Piñan Basualdo et al., "A microrobotic platform actuated by thermocapillary flows for manipulation at the air-water interface," *Sci. Robot.*, vol. 6, no. 52, 2021, Art. no. eabd3557.
[32] W. Wang et al., "Order and information in the patterns of spinning magnetic micro-disks at the air-water interface," *Sci. Adv.*, vol. 8, no. 2, 2022, Art. no. eabk0685.
[33] J. Zhang, M. Salehizadeh, and E. Diller, "Parallel pick and place using two independent untethered mobile magnetic microgrippers," in *Proc. IEEE Int. Conf. Robot. Automat.*, Brisbane, QLD, Australia, 2018, pp. 123–128.
[34] M. Salehizadeh and E. D. Diller, "Path planning and tracking for an underactuated two-microrobot system," *IEEE Robot. Autom. Lett.*, vol. 6, no. 2, pp. 2674–2681, Apr. 2021.
[35] S. Zhong et al., "Spatial constraint-based navigation and emergency replanning adaptive control for magnetic helical microrobots in dynamic environments," *IEEE Trans. Autom. Sci. Eng.*, vol. 21, no. 4, pp. 7180–7189, Oct. 2024.
[36] H. Wang et al., "Data-driven parallel adaptive control for magnetic helical microrobots with derivative structure in uncertain environments," *IEEE Trans. Syst. Man Cybern., Syst.*, vol. 54, no. 7, pp. 4139–4150, Jul. 2024.
[37] S. Zhong et al., "Double-modal locomotion of a hydrogel ultra-soft magnetic miniature robot with switchable forms," *Cyborg Bionic Syst.*, vol. 5, Jan. 2024, Art. no. 0077, doi: 10.34133/CBSYSTEMS.0077.
[38] Z. Wei et al., "Magnetic repulsion-based robot with diverse locomotion capabilities," *IEEE Robot. Autom. Lett.*, vol. 9, no. 1, pp. 398–405, Jan. 2024.
[39] P. A. Kralchevsky and K. Nagayama, "Capillary interactions between particles bound to interfaces, liquid films and biomembranes," *Adv. Colloid Interface Sci.*, vol. 85, no. 2-3, pp. 145–192, 2000.
[40] S. Zhu et al., "Dynamically reversible cooperation and interaction of multiple rotating micromotors," *Lab. Chip*, vol. 23, no. 7, pp. 1905–1917, 2023.
[41] Z. Gao, "Active disturbance rejection control: A paradigm shift in feedback control system design," in *Proc. Amer. Control Conf.*, Minneapolis, MN, USA, 2006, pp. 1–7.

Shihao Zhong received the B.S. degree in automation from North China University of Technology, Beijing, China, in 2021. He is currently working toward the Ph.D. degree in mechanical engineering with Beijing Institute of Technology, Beijing, China.

His research interest includes motion control of miniature magnetic robots.

Siyu Guo received the B.S. degree in mechanical engineering from Beijing Institute of Technology, Beijing, China, in 2021.

His research interest includes motion control of miniature magnetic robots.

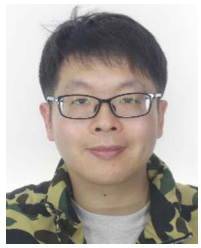

Tao Sun received the Ph.D. degree in mechanical engineering from Beijing Institute of Technology, Beijing, China, in 2016.

His research interests includes biomanipulation in micronano scale.

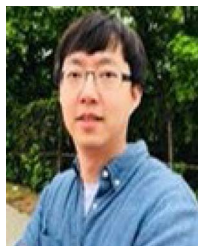

Hen-Wei Huang received the B.S. and M.S. degrees in mechanical engineering from National Taiwan University, Taipei, Taiwan, in 2011 and 2012, respectively, and the Ph.D. degree in robotics technology from ETH Zürich, Zürich, Switzerland, in 2018.

He is currently the Nanyang Assistant Professor with Nanyang Technological University. His research interests include robotics and translational medicine.

Qing Shi (Senior Member, IEEE) received the B.S. degree in mechatronics from Beijing Institute of Technology, Beijing, China, in 2006, and the Ph.D. degree in biomedical engineering from Waseda University, Shinjuku, Japan, in 2012.

He had been a Research Associate with GCOE Global Robot Academia, Waseda University from 2009 to 2013. He is currently a Professor with the School of Mechatronical Engineering, Beijing Institute of Technology. His research interests include focused on bioinspired and micro/nano robotics.

Qiang Huang (Fellow, IEEE) received the B.S. and M.S. degrees in electrical engineering from the Harbin Institute of Technology, Harbin, China, in 1986 and 1989, respectively, and the Ph.D. degree in mechanical engineering from Waseda University, Tokyo, Japan, in 1996.

He is currently a Professor with the Beijing Institute of Technology, Beijing, China. He is the Director with the Key Laboratory of Biomimetic Robots and Systems, Ministry of Education of China.

Toshio Fukuda (Life Fellow, IEEE) received the B.S. degree in engineering from Waseda University, Tokyo, Japan, in 1971, and the M.S. and Ph.D. degrees in engineering from the University of Tokyo, Tokyo, in 1973 and 1977, respectively.

He is currently a Professor Emeritus with Nagoya University, Nagoya, Japan, a Professor with Waseda University, Japan, where his research interests include intelligent robotic systems, cellular robotic systems, mechatronics, and micro/nano robotics.

Huaping Wang (Member, IEEE) received the B.S. degree in mechatronics and the Ph.D. degree in mechanical engineering from Beijing Institute of Technology, Beijing, China, in 2010 and 2015, respectively.

He has been a Professor with Beijing Institute of Technology since 2022. His research interests include micronano robotics, micronano manipulation, and automation at micronano scales.